Atmospheric Pollution Research 15 (2024) 102179

Contents lists available at ScienceDirect

Atmospheric Pollution Research

journal homepage: www.elsevier.com/locate/apr

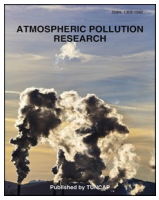

Analyzing the influence of the planetary boundary layer height, ventilation coefficient, thermal inversions, and aerosol optical Depth on the concentration of $PM_{2.5}$ in the city of São Paulo: A long-term study

Gregori de Arruda Moreira [a,b,*], Marcia Talita Amorim Marques [c], Fabio Juliano da Silva Lopes [b], Maria de Fátima Andrade [c], Eduardo Landulfo [b]

[a] Federal Institute of São Paulo (IFSP), São Paulo, Brazil
[b] Institute of Research and Nuclear Energy (IPEN), São Paulo, Brazil
[c] Institute of Astronomy, Geophysics and Atmospheric Sciences (IAG), São Paulo, Brazil

ARTICLE INFO

Keywords:
Planetary boundary layer
Remote sensing
$PM_{2.5}$
AOD
GLM

ABSTRACT

Cases of intense air pollution have been a recurring problem in most of urban centers in different regions of the world. Although actions to mitigate pollutant emissions are fundamental, it is also necessary to understand which factors can favor their dispersion process. In this scenario, this paper presents, for the first time, a long-term analysis of the Planetary Boundary Layer Height (*PBLH*), estimated through lidar and radiosounding data, Ventilation Coefficient (*VC*), Thermal Inversions (*TI*), and Aerosol Optical Depth (*AOD*), for the city of São Paulo, demonstrating how these variables are related with $PM_{2.5}$ concentration. The analyzes showed that *PBLH* and *VC* have a seasonal cycle, with higher values in summer and lower ones in winter. Furthermore, *PBLH* is affected by one local factor, the sea-breeze, which reduces the concentration of aerosols in the late afternoon, resulting in an underestimated *PBLH* obtained from lidar data. Furthermore, from AERONET data, a predominance of Black Carbon and small particles was observed in all seasons, which are associated with the feedback effect observed in winter. Such effect attenuates the increase of *PBLH* and *VC* in cases of high concentrations of $PM_{2.5}$. Finally, it was presented a Generalized Linear Model, which combines *VC*, *AOD* and *TI* information as input and can estimate the $PM_{2.5}$ concentration with a $R^2 = 0.93$.

1. Introduction

Air quality monitoring has become a crucial activity in recent years, particularly for megacities, due to the increasing level of pollutants in the atmosphere. (Dupont et al., 2016; Li et al., 2017, 2019; Kotthaus et al., 2018; Murthy et al., 2020).However, monitoring air quality is a complex task that requires continuous meteorological observations, such as wind speed, net radiation, pollutants concentration, and most importantly, the height of the planetary boundary layer (*PBLH*), which can strongly influence air pollution levels, because aerosols are predominantly situated in this tropospheric region (Li et al., 2017).

The lowermost tropospheric region is called Planetary Boundary Layer (*PBL*). This region is endowed with turbulent behavior, responding to surface forcings and being influenced by the earth's surface on a time scale equal to or lower than 1 h (Stull, 1988). Such a layer is characterized by the high variability of its height (*PBLH*) during the daily cycle. Considering an ideal scenario, some instants after sunrise, the positive net radiation causes the increase of ground surface temperature, so that the air masses (located at low heights) are warmed. This phenomenon, together with turbulent mixing, favors the convective process, resulting in the warming of the upper region of the troposphere and originating an unstable sublayer denominated Convective Boundary Layer (*CBL*) or Mixing Layer (*ML*). Close to sunset, convection ceases, and the *CBL* becomes a neutrally stratified layer denominated Residual Layer (*RL*). This layer contains the main characteristics of the previous *CBL*. Parallel to this process, from the ground emerges a sublayer, endowed with stability, called Stable Boundary Layer (*SBL*) (Stull, 1988).

In addition to variations in height values caused by the daily cycle, which is directly influenced by atmospheric stability, *PBL* H can also be

Peer review under responsibility of Turkish National Committee for Air Pollution Research and Control.
* Corresponding author. Federal Institute of São Paulo (IFSP), São Paulo, Brazil.
E-mail address: gregori.moreira@ifsp.edu.br (G.A. Moreira).

https://doi.org/10.1016/j.apr.2024.102179
Received 19 December 2023; Received in revised form 3 April 2024; Accepted 7 May 2024
Available online 10 May 2024

affected by the behavior of other forcings, which can be attenuators of the dispersion process, due to the negative result caused in mixing/growth process. The reduction in sensible heat due to intense aerosol backscattering, can reduce the air temperature and weaken the turbulent mixing process. Such a process results in a stabilized *PBL*, which is endowed with a low height and a high concentration of pollutants in its lower region (Li et al., 2017). Thermal Inversions (*TI*) can attenuate the dispersion process, trapping the pollutants in the regions below its top. So that several extreme pollution episodes are associated with *TI* at the *PBL* top (Wallace J and Kanaroglou, 2009; Liu et al., 2019; Xu et al., 2019; Guo et al., 2020). Overall, understanding the behavior of the *PBL* and its influencing factors is crucial in monitoring and mitigating air pollution levels, particularly in megacities.

However, although it is essential to monitor PBLH variations, it is not an easy task. Such a variable can be estimated from the direct observations of vertical profiles of turbulent quantities (Teixeira et al., 2021) or retrieved indirectly from variations in the vertical profile of some variables, such as temperature, relative humidity, wind speed, and aerosol concentration (Stull, 1988).

The method most widely applied in *PBL* H detection is radiosounding. However, due to low spatial (~300 m) and temporal (~12 h) resolution, this technique does not allow monitoring the variation of *PBLH* throughout the day (Li et al., 2017). To solve this problem, remote sensing systems such as elastic lidar (Toledo et al., 2017; Bravo-Aranda et al., 2017; Moreira et al., 2018, 2022), Doppler lidar (Manninen et al., 2018; Marques et al., 2018; Moreira et al., 2019), radar wind profiler (Liu et al., 2019; Solanki et al., 2022; Salmun et al., 2023), ceilometers (Caicedo et al., 2017; Lee et al., 2019; Uzan et al., 2020; Moreira et al., 2020) and microwave radiometer (Bravo-Aranda et al., 2017; Moreira et al., 2020), have been broadly applied in the *PBLH* detection during the last decade. Such systems are endowed with high temporal and spatial resolution so that it is possible to track the *PBLH* evolution throughout its daily cycle.

From lidar data, Dupont et al. (2016) estimated the *PBLH* evolution in Paris (France), and demonstrated that during extreme pollution events, such a variable can influence the $PM_{2.5}$ concentration. Miao and Liu (2019) analyzed the behavior of the *PBLH* and $PM_{2.5}$ concentration in 28 air quality stations across of China and identified that the correlation between these variables increases as higher $PM_{2.5}$ concentrations are detected. Lou et al. (2019) analyzed the relationship between PM2.5 and PBLH in three different PBL regimes (neutral, stable, and convective), identifying that the correlation signal is directly associated with these regimes, being that negative correlations were observed during convective and neutral regimes, and positive correlation during the stable period. From a combination between *PBLH* (obtained from microwave radiometer data) and wind speed, Moreira et al. (2020) estimated the ventilation coefficient (*VC*) and demonstrated that such a variable positively influences the dispersion of Black Carbon in Granada (Spain). Murthy et al. (2020), from ceilometer data, estimated the *PBLH* evolution in Delhi (India) and presented a negative correlation between $PM_{2.5}$ concentration and *PBLH*, mainly during convective periods.

In this study, the primary objective is to investigate how *PBLH*, *VC*, *TI* occurrence and the variations in some atmospheric optical properties (e.g., Atmospheric Optical Depth - *AOD*) can affect the $PM_{2.5}$ concentration in São Paulo city during the convective period. Therefore, first a description of the seasonal behavior of these variables will be presented. Next, it will be described how they relate to each other, whether or not they may favor dispersion processes. And finally, a way to relate such variables with the concentration of $PM_{2.5}$ using a Generalized Linear Model (*GLM*) will be presented. It is important to highlight that is the first long term study relating *PBLH* and $PM_{2.5}$ concentration performed in this region. This paper is organized into five sections. Section 2 provides an overview of the study area, the equipment used for measurements, and the campaigns conducted for data collection. Section 3 describes the methodology employed in the study and the algorithms used for data analysis. In Section 4, the results of the study are presented, and the implications of the findings are discussed. Finally, in Section 5, the main conclusions drawn from the study are summarized.

2. Materials

2.1. Study area

With around 12.8 million inhabitants (IBGE, 2022) and a vehicle fleet of around 32 million (São Paulo Municipality, 2020), São Paulo is the most populous Brazilian city. This city has a humid subtropical climate, where summer is warm and humid, winter is dry and with low decrease in the average temperature. On the other hand, similar intermediate climatic characteristics are observed in spring and autumn (CETESB, 2019). Fig. 1c shows the places where the LIDAR is located (Center of Laser and Applications (*CELAP*) – violet star) and the radiosoundings where launched (Campo de Marte Airport – orange star), as well as, all CETESB stations, at São Paulo municipality, where $PM_{2.5}$ is measured (colored circles).

2.2. SPU-Lidar Station

The SPU-Lidar Station São Paulo Lidar Station is a multiwavelength elastic lidar system installed in the *CELAP* (23°33′38″ S, 46°44′23″ W, 760 m a.s.l.) (Fig. 1c – violet star) and is part of LALINET (http://lalinet.org), a federative coordinated lidar network that focuses on monitoring the vertical distribution of particle optical properties in Latin America. This system works with a pulsed Nd:YAG laser, pointed to zenith direction and that emits radiation at four wavelengths (355, 532, and 1064 nm) with a repetition rate of 10 Hz. The data acquisition occurs by three Raman-shifted (387, 408, and 530 nm) and three elastic (355, 532, and 1064 nm) channels. SPU-Lidar Station has a spatial resolution of 7.5 m, reaching the full overlap at 300 m a.g.l. (Lopes et al., 2019; Moreira et al., 2019). For this work, all lidar measurements were obtained from the wavelength of 532 nm (elastic), with a temporal resolution of 1 min, from January 2013 to December 2019, from 13 UTC to 21 UTC (this period corresponds to 10 to 18 Local time).

2.3. Radiosoundings

The radiosoundings were launched daily at Campo de Marte Airport (23° 41′ S, 46° 53' W) (Fig. 1c – orange star) at 12 and 00 UTC (09 and 21 Local time, respectively). In this paper, only the 12 UTC data (collected from January 2013 to December 2019) were used, so that from them were estimated the *PBLH* (Section 3.1.2) and the Thermal Inversions properties (Section 3.4).

2.4. Aerosol Robotic network

The Aerosol Robotic Network (*AERONET*) is a network dedicated to terrestrial monitoring and characterization of aerosols at a regional and global level. (Holben et al., 1998). In this paper the values of Aerosol Optical Depth (*AOD*), Ångström Exponent (*AE*), Lidar Ratio (*LR*) and Angström Exponent of Scattering and Absorption were obtained from *AERONET* São Paulo Station (23° 33′ S, 46° 38' W) (Fig. 1c – red star). In this paper the *AERONET* data were collected from January 2013 to December 2019.

2.5. Surface wind speed

The hourly horizontal wind speed (*HWS* [ms^{-1}]) were obtained from the *CETESB* Pinheiros station (Fig. 1c – yellow circle), from January 2013 to December 2019.

2.6. $PM_{2.5}$ hourly concentration

Hourly records of fine particulate matter ($PM_{2.5}$ [μgm^{-3}]) were

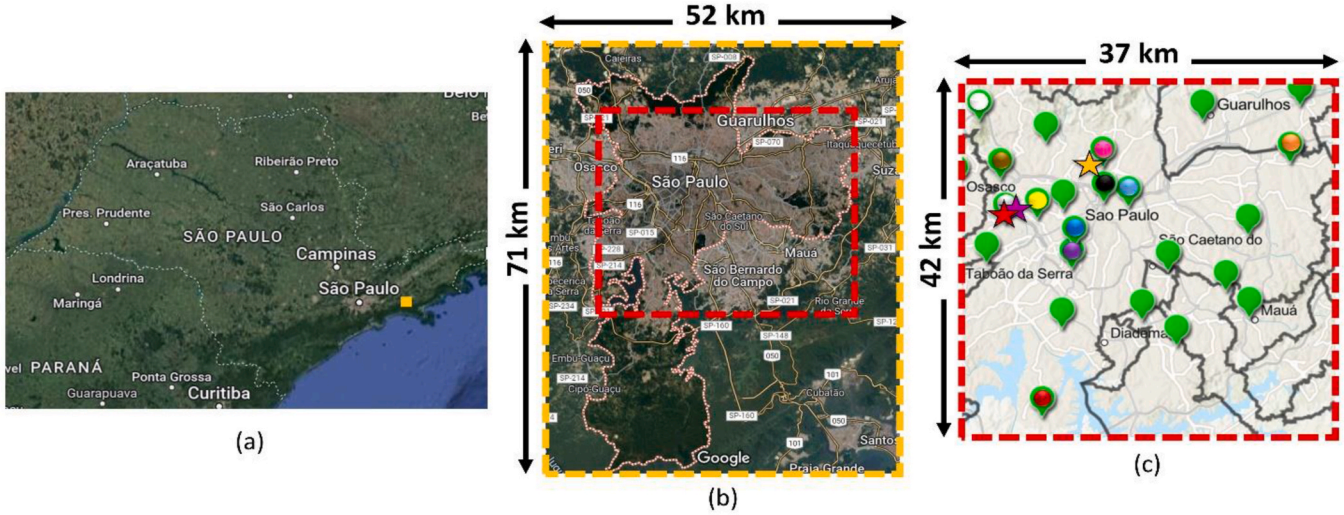

Fig. 1. (a) São Paulo state and São Paulo city location (yellow square). (b) São Paulo city in detail and region where the data were collected (red square). (c) The red, violet and orange stars represent the AERONET São Paulo Station, Center of Laser and Applications (*CELAP*), and the Campo de Marte Airport, respectvely. The green balloons represent the São Paulo Environmental Company (*CETESB*) stations located in São Paulo city and some neighboring municipalities. The colored circles represent all *CETESB* stations located in São Paulo municipality where $PM_{2.5}$ is measured.

collected from all *CETESB* stations located in São Paulo Municipality where such a pollutant is measured (colored circles in Fig. 1c). In order to be more representative and addressing the different characteristics of each São Paulo municipality region, the $PM_{2.5}$ hourly concentration values presented in this paper correspond to average value of all stations. These data were collected from January 2013 to December 2019.

3. Methods

3.1. PBLH detection

3.1.1. Lidar

The lidar signal was pre-processed by the three-step correction (D'Amico et al., 2016). Firstly, to reduce the influence of the electrical noise, the dark current signal ($DC(z)$) is subtracted from the raw signal ($P(z)$). In the second step the background radiation signal (BG) is removed to attenuate the influence of external sources. Then, the value obtained from the two previous steps is multiplied by the square of the corresponding height (z), due to attenuation of signal with the height. Finally, is obtained the Range Corrected Signal (RCS):

$$RCS(z) = (P(z) - DC(z) - BG) * z^2 \quad (1)$$

After this correction, the PBLH is estimated from the Wavelet Covariance Transform Method (WCT) (Baars et al., 2008). In this method, a covariance (W) is performed between the average RCS obtained during 1 h ($\overline{RCS}(z)$) and a mother-wavelet, which in this case is the Haar function ($h(a,b)$).

$$W(a,b) = \frac{1}{a}\int_{a}^{b} \overline{RCS}(z) h dz \quad (2)$$

where a and b are respectively the values of dilatation and transition-related to the mother-wavelet, b is the height above the ground, and z_i and z_f are the respective lower and upper limit of the $\overline{RCS}$ (z). The height with maximum in $W(z)$ corresponds to sharpest drop in the $\overline{RCS}$ (z), therefore is a height characterized by high reduction in the aerosol concentration, or in other words, is the transition between the *PBL* and the Free Troposphere (Baars et al., 2008). The values of a and b applied in this paper are respectively 200 and 40 m. Such values were obtained by Moreira et al. (2022) during two comparison campaigns between the *PBLH* obtained from radiosounding and elastic lidar data in São Paulo.

3.1.2. Radiossounding

The *PBLH* obtained from radiossounding data was estimated from the Parcel Method (Holzworth, 1964). Such a method considers the *PBLH* as the altitude whose an air parcel with an ambient temperature T can adiabatically rise from the ground by convection. Therefore, from the vertical potential temperature profile ($\theta(z)$), the *PBLH* is the first height z endowed of $\theta(z)$ equal to potential temperature at surface level ($\theta(z_0)$).

In order to observe a longer period of *PBL* evolution, and considering the results of previous works in which the *PBLH* estimated by lidar and radiosoundings were compared and shown to be equivalent (Moreira et al., 2014, 2022; Marques et al., 2018), the results of lidar and radiosonde were combined, so that in time series presented in the next sections, the *PBLH* value at 12 UTC was estimated from radiosonde data, while for the other times (13–21 UTC) the results were estimated from lidar data.

3.2. PBLH long term analysis

The *PBLH* long term analysis is presented in section 4 and it includes the seasonal hourly distribution, as well as, the mean and maximum ($PBLH_{Max}$) values. In addition, the *PBLH* Growth Rate ($PBLH_{GR}$) was estimated. Such a variable is calculated from the slope of a linear fit between the first *PBLH*, estimated for the day, and the last point to reach 90% of the daily *PBLH* maximum (Moreira et al., 2020). In addition, it will be performed a trend analysis of the daily $PBLH_{Max}$ based on Sen's estimator (Sen, 1986), from which will be possible to estimate the Sen's slope and consequently identify a non trend, an upward trend or downward trend.

3.3. Ventilation coefficient

The ventilation coefficient (VC) is the product between the *PBLH* (m) and the *HWS* (ms^{-1}) near the surface, as indicated by the following equation:

$$VC = PBLH * HWS \quad (3)$$

The VC indicates the efficiency of pollutant dispersion; therefore, it plays an important role in air quality studies (Nair et al., 2007; Lu et al.,

2012). Higher values of *VC* indicate favorable conditions to the dispersion of pollutants, while lower ones can result in higher pollutant concentrations. The hourly values of *PBLH*, estimated from lidar measurements (section 3.1.1), and surface horizontal wind speed, obtained at Pinheiros station (section 2.4), were used to calculate *VC* values.

3.4. Thermal inversions

The Thermal Inversions (*TI*) occurs when a layer of cool air is overlain by a layer of warmer air, contrary to the traditional process, in which the temperature is reduced as the height increases (Stull, 1988). Such phenomena were estimated from the vertical temperature profile ($T(z)$) of radiosoundings launched at 12 UTC (09 local time). All *TI* were classified in Surface Based Inversion (*SBI*) (when the base of inversion is located at the surface) or Elevated Inversion (*EI*), which occurs when the base of inversion is above the surface, using the methodology described in Abdul-Wahab et al. (2004).From this classification the following parameters were calculated: *SBI*/*EI* Depth [SBI/EI_{Depth}] (the deep/height of the *SBI*/*EI*), *SBI*/*EI* Intensity [SBI/EI_{Int}] and *SBI*/*EI* occurrence [SBI/EI_{Occur}] (the percentage of days where at least one *SBI*/ *EI* case is identified considering only the days where radiosounding was launched). In addition, it was performed a statistical analysis (section 4.2)

3.5. Aerosol classification by AERODOG

The AERONET Data Organization & Graphics (*AERODOG*) algorithm, developed by Lopes (Lopes, 2021), utilizes *AERONET* data and the optical properties of aerosols, such as *AOD*, *A*), and *LR*, to provide an atmospheric aerosol classification based on results obtained in previous works such as Cazorla et al. (2013) and Romano et al. (2019). The algorithm includes a python script available in the GitHub repository, which can organize *AERONET* directsun and inversion data using level 1.5 or 2.0. The algorithm is licensed under the Creative Commons License, and more details can be found in Lopes (2021).

4. Results and discussion

4.1. PBLH evolution in São Paulo city

Fig. 2 displays the diurnal variation of the *PBLH* in São Paulo city from 12 to 21 UTC. Despite the hourly values exhibiting high variability, the mean values exhibit a well-defined daily cycle, characterized by a sharp increase between 12 and 17 UTC, culminating in the maximum average value of [1416 ± 429] m at 18 UTC. Subsequently, the *PBLH* mean value remains relatively constant until 21 UTC.

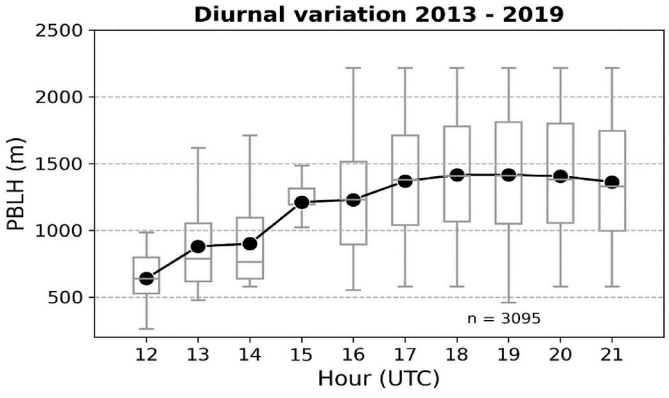

Fig. 2. Diurnal variation of *PBLH* (m) for the whole period (March 2013 to November 2019) estimated from radiosounding (12 UTC) and lidar (13–21 UTC) data (grey boxes and black dots). The boxes show the 1st (lower edge), 2nd (inside line), and 3rd (upper edge) quartiles of the distribution, and whiskers indicate the minimum and maximum values, disregarding those beyond the inner fences (not shown in the graph). Black circles indicate mean values, and n (lower right corner) is the number of valid hours for the period.

Fig. 3 presents the seasonal *PBLH* behavior, wherein summer (Fig. 3d) exhibits the lowest number of measurement hours (n = 219) due to the high rainfall rate characteristic of the humid subtropical climate, which renders lidar measurements unfeasible. Conversely, winter (Fig, 3b), the dry season, has the highest number of measurements (1122 h).

Considering the average values, the higher hourly values are observed during summer (Fig. 3d) while the lower ones occur during winter (Fig. 3b). Similar findings also have been reported in cities with different latitudes like as: Leipzig (Baars et al., 2008), Jülich (Schween et al., 2014), Palaiseau (Pal and Haeffelin, 2015), and Granada (Moreira et al., 2020).

In autumn (Fig. 3a), the *PBLH* increases continuously from 12 until 18 UTC, when the maximum average value of [1540 ± 330] m is reached. Then *PBLH* remains quite constant until 20 UTC and presents an apparent decrease at 21 UTC (~203 m), which is caused by the influence of the sea breeze. According to Oliveira et al. (2003), the sea breeze affects the plateau "Paulista" more than 50% of all days in a year, causing an intense decrease in air temperature and an increase in relative humidity and wind speed, as well as, a shift in wind direction from northeast to southeast bringing colder and moist air from the coast to the continent, and causing a reduction in aerosol concentration at specific heights. As a result, it is generated a sharp drop in the *RCS* profile, as can be observed in Fig. 4 from 19 Local Time, resulting in the *PBLH* underestimation by *WCT* (Moreira et al., 2022). This variation in *PBLH* during the late afternoon in São Paulo city was also observed by Ribeiro et al. 2018 and Sánchez et al. (2020) using radiosonde data. In addition, during the autumn the $PBLH_{Gr}$ is [100 ± 80] mh^{-1}.

During winter, the *PBLH* growths continuously from 12 until 19 UTC, when it reaches the maximum average value of [1400 ± 442] m (Fig. 3b). After this period, the *PBLH* remains relatively constant ([1410 ± 430] m) until 21 UTC. The $PBLH_{Gr}$ during this season is the lower one observed, [70 ± 50] mh^{-1}.

In spring (Fig. 3c), the *PBLH* has an intense growth from 12 until 17 UTC, reaching its maximum value ([1490 ± 430] m). Then, it remains constant until 18 UTC, and shows a slight decrease (105 m) until 21 UTC. This apparent decrease in *PBLH* can be attributed to the sea breeze effect, which, as mentioned before, causes the *WCT* underestimate the *PBLH*, due to the sharp drop in the vertical aerosol profile. During this season the $PBLH_{Gr}$ is [100 ± 90] mh^{-1}, quite similar to value observed during Autumn.

Compared to other seasons, Summer (Fig. 3d) has the more intense $PBLH_{Gr}$ ([110 ± 90] mh^{-1}). During this season the *PBLH* growths quite constantly from 12 until 19 UTC, has a small apparent reduction at 20 UTC and increases again at 21 UTC, where the maximum average value ([1600 ± 500] m) is observed.

Fig. 5 illustrates the trend analysis to daily $PBLH_{Max}$. Summer (Fig. 5a) and autumn ((Fig. 5b) no have a significative trend, what means that throughout the period analyzed there was no tendency for the value of $PBLH_{Max}$ to increase or decrease over the years. On the other hand, winter (Fig. 5c) and spring (Fig. 5d) have a positive value for the Sen Slope (0.29 myr^{-1} and 0.20 myr^{-1}, respectively) indicating that throughout the analyzed period there was a tendency for an increase in the $PBLH_{Max}$ value of 0.29 m per year in winter and 0.20 m per year in spring. However, other meteorological variables, not addressed in this study, need to be analyzed to justify such behaviors.

4.2. Thermal inversions Statistics

Table 1 presents a heatmap with the *SBI* and *EI* seasonal description to São Paulo municipality. The *SBIs* are endowed of seasonality being

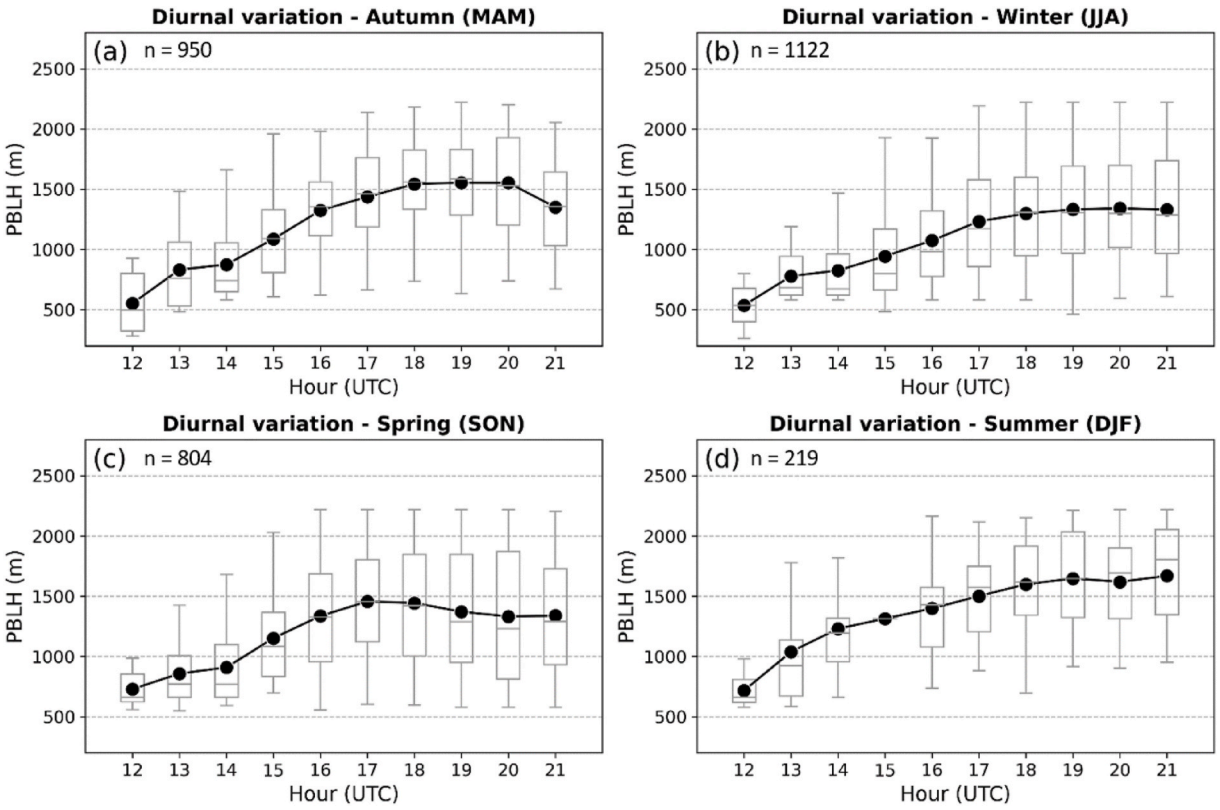

Fig. 3. Diurnal variation of *PBLH* (m) for the whole period (March 2013 to November 2019) estimated from radiosounding (12 UTC) and lidar (13–21 UTC) data (grey boxes and black dots). The grey boxes show the 1st (lower edge), 2nd (inside line), and 3rd (upper edge) quartiles of the distribution, and whiskers indicate the minimum and maximum values, disregarding those beyond the inner fences (not shown in the graph). Black circles indicate mean values, and n (lower right corner) is the number of valid hours of lidar measurements for each season. During the summer there are no *PBLH* values for midday local time (15 UTC) because of high incidence of sunlight in the lidar system.

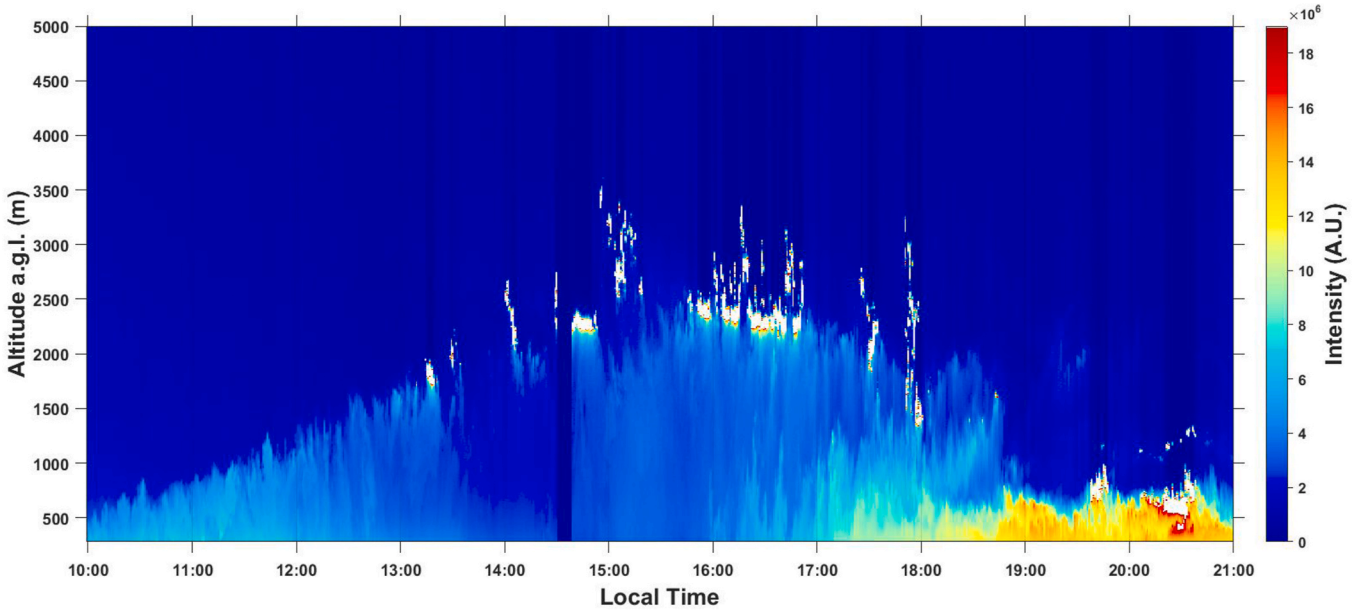

Fig. 4. Example of Sea-Breeze effect on lidar signal. São Paulo February 23, 2013. This case is deeply analyzed in Moreira et al. (2022); Sánchez et al. (2020).

more recurrent in winter (34.9% of days) and with low occurrence in summer (8.9 % of days). Similar results were observed in Oman (Abdul-Wahab et al., 2004). All seasons have similar *TI* intensities with [2.73 ± 0.01] °C in autumn and winter, and [2.72 ± 0.01] °C in summer and spring. Regarding the Deep, summer has the deepest *SBI* (373 ± 197) m, while the winter has the shallowest *SBI* (285 ± 110) m.

In the same way as *SBIs*, the *EIs* have a seasonal behaviour with higher occurrence in winter (57.8% of days) and lower one in summer (47.4% of days). Considering that at 12 UTC (09 a.m. Local Time) all seasons have an average *PBLH* value lower than 1 km, Table 1 presents

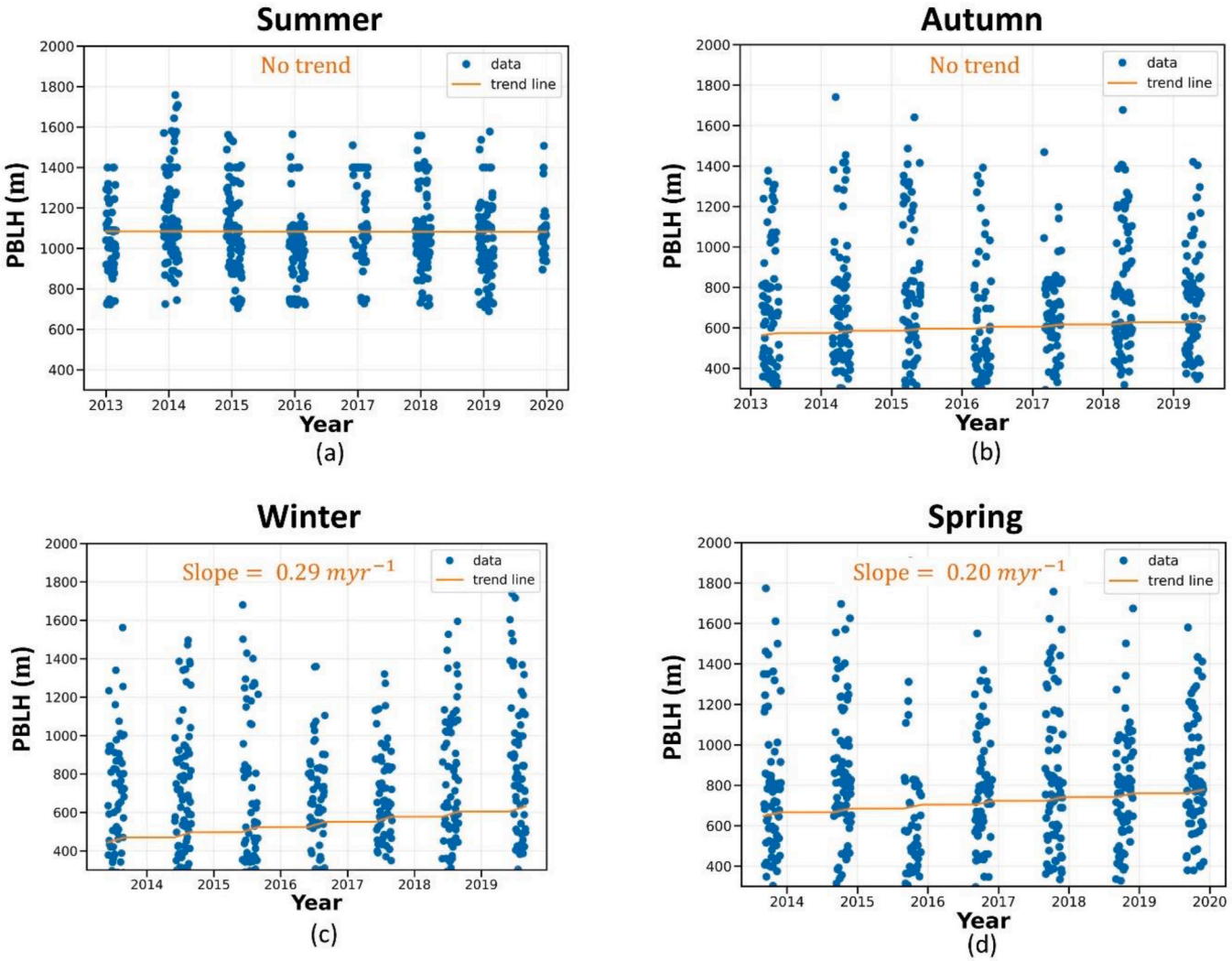

Fig. 5. Trend analyzes of the daily $PBLH_{Max}$ for the whole period (March 2013 to November 2019).

Table 1
TI seasonal description to São Paulo city. The color scale varies linearly from dark green to red, which represent the lowest and highest values, respectively.

SEASONS	SBI			EI					
	Depth (m)	Int (°C)	Ocurr. (%)	Depth (m)	Int ($°C^{-1}$)	Ocurr. (%)			
						All	Below 1 km	Between 1 and 2 km	Above 2 km
Summer	373 ± 197	2.72 ± 0.01	8.9	245 ± 78	2.74 ± 0.01	47.4	32.8	8.0	59.2
Autumn	307 ± 121	2.73 ± 0.01	18.4	247 ± 79	2.74 ± 0.01	54.9	34.3	16.0	49.7
Winter	285 ± 110	2.73 ± 0.01	34.9	261 ± 89	2.74 ± 0.02	57.8	31.8	21.7	46.5
Spring	315 ± 143	2.72 ± 0.02	13.3	255± 85	2.74 ± 0.11	56.8	37.5	19.2	43.3

the occurrence of *EI* with base situated below 1 km (therefore inside the *CBL*) between 1 and 2 km, and above 2 km. Spring and winter are the seasons with more (37.5 %) and less (31.8 %) *EI* with base in the *CBL* region, respectively. On the other hand, Summer and winter are the seasons with less (8.0 %) and more (21.7 %) *EI* base situated between 1 and 2 km. Finally, the *EI with base* above 2 km, which tend to have less influence on the development of *PBLH*, are predominant in summer (59.2 %). Therefore, winter is the season with the highest occurrence of inversions, and it is possible to state that most of them occur either within the *CBL* or close to its top. Such an event tends to attenuate the

growth of *CBL*, disadvantaging pollutant dispersion processes. In addition, winter is the season with the deeper *EI* ([261 ± 89] m). Regarding the intensity, all seasons have the same average value (2.74 °C).

4.3. Characterization of aerosol composition from AERONET data

Fig. 6 provides a comprehensive analysis of the seasonal aerosol composition in São Paulo city. In all seasons, small particles with low absorption dominate, while black carbon (*BC*), which is characterized by high absorption is present throughout. Autumn (Fig. 6a) is characterized by a combination or a mix of dust, *BC* and brown carbon (*BrC*) pollutants. The Spring season (Fig. 6c) exhibits a mix of large particles and other pollutants, including a combination of *BrC* and *BC*. Summer (Fig. 6d) is similar to spring in terms of aerosol composition, except for the detection of large particles (negative Single Scattering Albedo [*SSA*]) of the mix Dust, *BC* and *BrC*. Winter (Fig. 6b) features a range of aerosol types observed in other seasons, with a predominance of fine particles (positive *SSA*).

4.3.1. PBLH and AOD

Although the *PBL* can exhibit various heights at different *AOD* values (Fig. 7), the mean values suggest a negative correlation between *PBLH* and *AOD*. In other words, as the *PBLH* decreases, the *AOD* increases. Similar findings have also been reported by Chen et al. (2022).

The seasonal characterization of *PBLH* and aerosols presented in sections 4.1 and 4.2, respectively, indicates that lower *PBLH* are observed during winter, which is characterized by the presence of *BC* aerosol type and other fine particles. Therefore, it is reasonable to assume that there is a relation between *PBLH*, aerosol loading, and *AOD*, so higher *AOD* values represent higher aerosol concentrations (in the case of São Paulo, the absorption aerosol is *BC*).

4.4. Influence of PBLH, VC and TI in the $PM_{2.5}$ concentration

The $PM_{2.5}$ concentration, *PBLH* and *VC* daily cycles to São Paulo city are presented in Fig. 8. *VC* has a daily cycle similar to *PBLH*, with lower values at early morning, maximum values during the center of the day, however while *PBLH* tends to maintain a constant value after reaching the daily maximum value, the *VC* decreases due to variation in the *HWS*. Although between 12 and 14 UTC $PM_{2.5}$ is anti-correlated with *PBLH* and *VC* (probably due to high growth rate of both variables, which favors the pollutant dispersion), from 15 to 18 UTC the variation of these three variables has the same positive signal, what probably is caused by the intense vehicular traffic during this period (São Paulo Municipality, 2021), which results in such a high emission level that even with favorable dispersion conditions, the concentration of pollutants continues to increase. At 19 UTC when the *VC* decreases and *PBLH* stays quite constant, the dispersion capacity of low troposphere reduces significantly. These factors combined with the begin of rush hour (São Paulo Municipality, 2021) result in an increase of $PM_{2.5}$ concentration.

Fig. 9 demonstrates the seasonal behavior of the $PM_{2.5}$ daily cycle and how it is influenced by *PBLH* and *VC*. $PM_{2.5}$ has a seasonal behavior

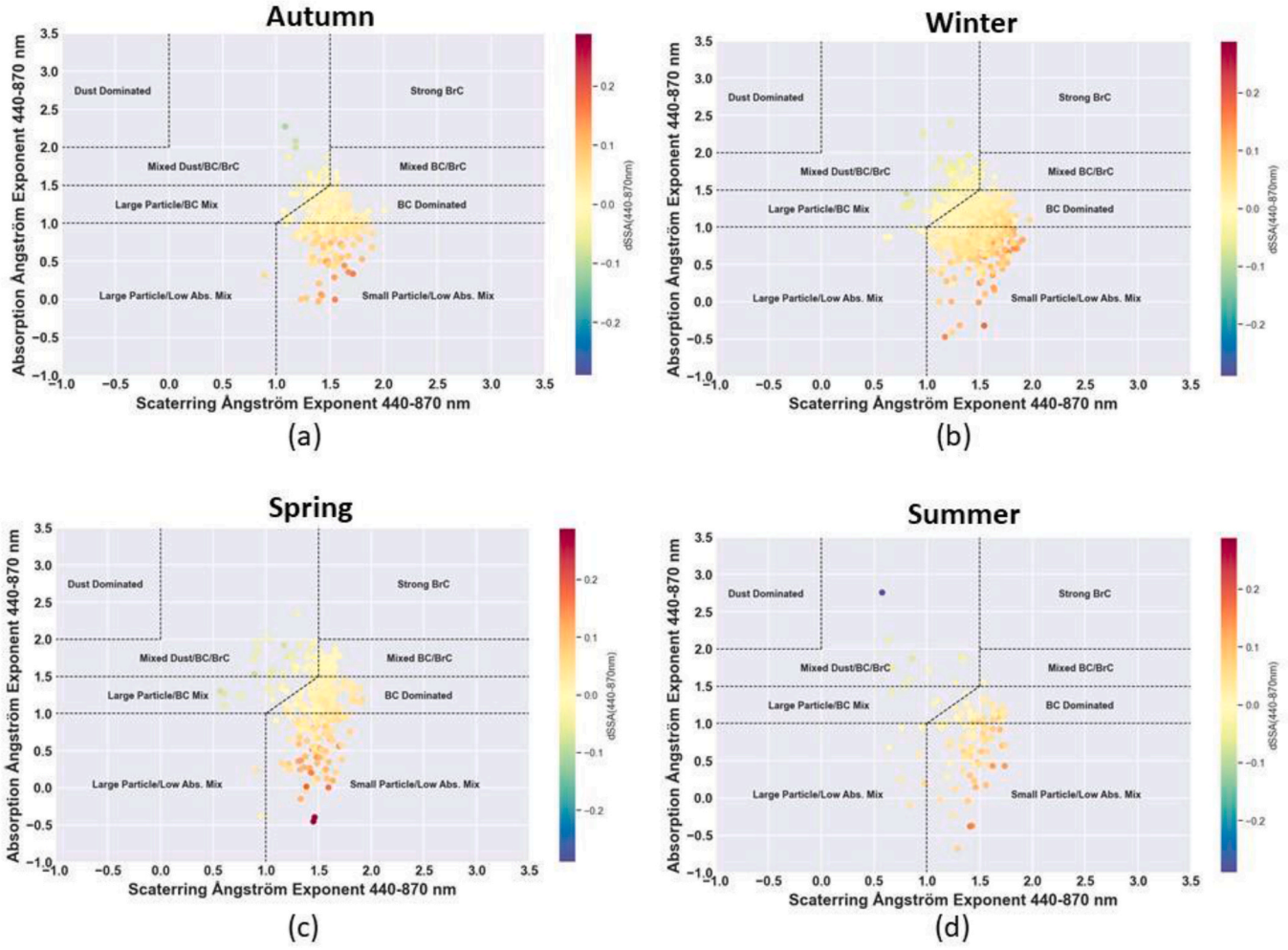

Fig. 6. Aerosol classification to São Paulo city during the (a) autumn, (b) winter, (c) spring and (d) summer obtained from *AERONET* data collected from 2012 to 2019 provided by the AERODOG script.

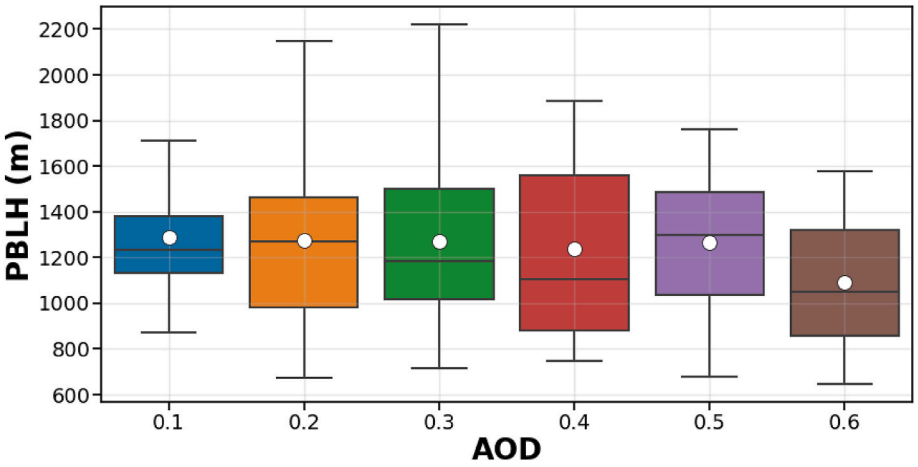

Fig. 7. Variation of *AOD* and *PBLH* for the whole period (March 2013 to November 2019) estimated from lidar data (grey boxes and black dots). The boxes show the 1st (lower edge), 2nd (inside line), and 3rd (upper edge) quartiles of the distribution, and whiskers indicate the minimum and maximum values, disregarding those beyond the inner fences (not shown in the graph). White circles indicate mean values, and n (lower right corner) is the number of valid hours for the period.

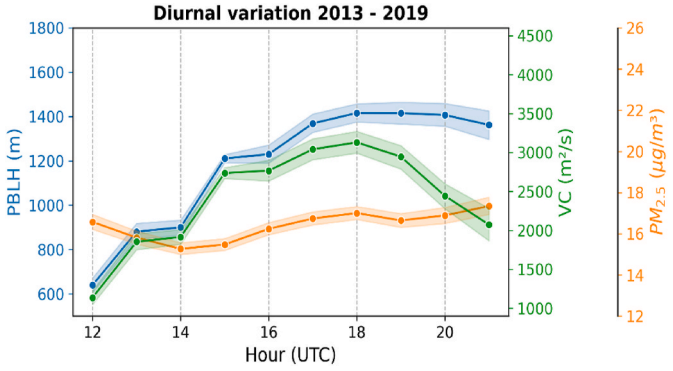

Fig. 8. Diurnal variation (14:00–21:00 UTC) for the whole period (March 2013 to November 2019) of *PBLH* (blue), *VC* (green) and $PM_{2.5}$ concentration (orange). Shaded regions show 95% confidence intervals.

with the higher average values in winter (Fig. 9b) and lower ones in summer (Fig. 9d). One of the main factors that result in high $PM_{2.5}$ concentration observed during winter, in comparison with other seasons, are the several biomass-burning episodes that occur in Brazilian central-west and Amazon region and affects São Paulo city (Moreira et al., 2021). Such factor combined with the reduced dispersions capability (due to lower *PBLH* and *VC* in comparison with other seasons) can elevate significantly the $PM_{2.5}$ levels. In addition, the high concentration of aerosols during the winter can influence the values of *VC* since aerosols weaken the surface winds, which consequently reduces the *VC* and the capability of pollutant dispersion in that region.

Excepting for winter, where an anti-correlation can be clearly observed, *VC* and $PM_{2.5}$ do not present a uniform relationship, so they are anti-correlated during the period of intense *VC* growing and positively correlated during the rest of the day. During the autumn (Fig. 9a) and spring (Fig. 9c), the correlation between $PM_{2.5}$ and *PBLH* is similar to that observed with *VC*. It is essential to highlight that the apparent reduction of the *PBLH* is caused by the presence of the sea breeze, which affects the detection of *PBLH* by lidar systems due to the decrease in the concentration of aerosols. Consequently, this phenomenon also affects the $PM_{2.5}$ concentration resulting in the reductions observed at the end of the day. Winter (Fig. 9b) and summer (Fig. 9d) present an anti-correlation between $PM_{2.5}$ and *PBLH*, when the highest $PBLH_{Gr}$ are observed, however when the daily $PBLH_{Max}$ is reached and the *PBLH* presents a small variation, the $PM_{2.5}$ concentration continues to increase (winter) or remains practically constant (summer).

Excepting autumn, in all seasons the $PM_{2.5}$ concentration begins to increase or stop to decrease at 16 UTC (in autumn at 15 UTC), although the *VC* continues increasing. This phenomenon may be associated with photochemistry activity, which leads to a higher secondary aerosol formation, mainly during the central part of the day (Seinfeld and Pandis, 2016; Pan et al., 2019).

Fig. 10 presents the trend analyzes of the daily maximum value of $PM_{2.5}$. All seasons have a significative negative Sen Slope, what indicates that throughout the analyzed period there was a tendency for a reduction in the maximum daily value of $PM_{2.5}$. Summer and Spring are the seasons with lower (-0.003 µg $m^{-3}.yr^{-1}$) and higher (-0.006 µg $m^{-3}.yr^{-1}$) $PM_{2.5}$ decrease rate. It is important to highlight that winter and spring are the unique seasons with a tendency for an increase in the $PBLH_{Max}$ value, are the seasons with the more intense $PM_{2.5}$ maximum daily value decrease. Similar results, associated with a tendency to reduce $PM_{2.5}$ concentration, results also were observed in China (Bai et al., 2019; Li et al., 2023), Eastern and Western Europe (Li et al., 2019).

Table 2 presents the seasonal average values of the minimum ($PM_{2.5}^{Min}$), mean ($PM_{2.5}^{Mean}$) and maximum ($PM_{2.5}^{Max}$) daily $PM_{2.5}$ concentrations in the presence or absence of *TI*. Excepting autumn, all seasons have a higher $PM_{2.5}$ concentration when a *TI* was registered, so that the higher difference occur with $PM_{2.5}^{Max}$ in winter, when the value registered during the days endowed of *TI* is around 30% higher than when no *TI* is observed. Such result is directly associated with the influence of *TI* in the *PBLH*, which can attenuate the growth rate resulting in reduction of dispersion capability.

4.5. Combining multiple variables to understand the variations in $PM_{2.5}$ concentrations

In order to try to estimate a direct correlation between meteorological variables and the concentration of $PM_{2.5}$, the correlation of the average daily concentrations of this pollutant with the average daily values of *PBLH* and *VC* was initially analyzed. Table 3 presents the seasonal Pearson's correlation to $PM_{2.5}$ - *VC* and $PM_{2.5}$ – *PBLH*. The *PBLH* presents a small correlation with $PM_{2.5}$ concentration, so that the highest significative absolute value is observed during the autumn (-0.14), and the lower one during the winter (-0.05). The correlation during the summer is 0.01, however it does not present a significative p-value. Luan et al. (2018) observed that the correlation between *PBLH* and $PM_{2.5}$ concentration becomes higher as $PM_{2.5}$ mass increases (mainly in concentrations higher than 150 µgm^{-3}). Xiang et al. (2019) observed that *PBLH* and $PM_{2.5}$ concentration does not present a significant correlation under low $PM_{2.5}$ conditions, so that significant concentrations only

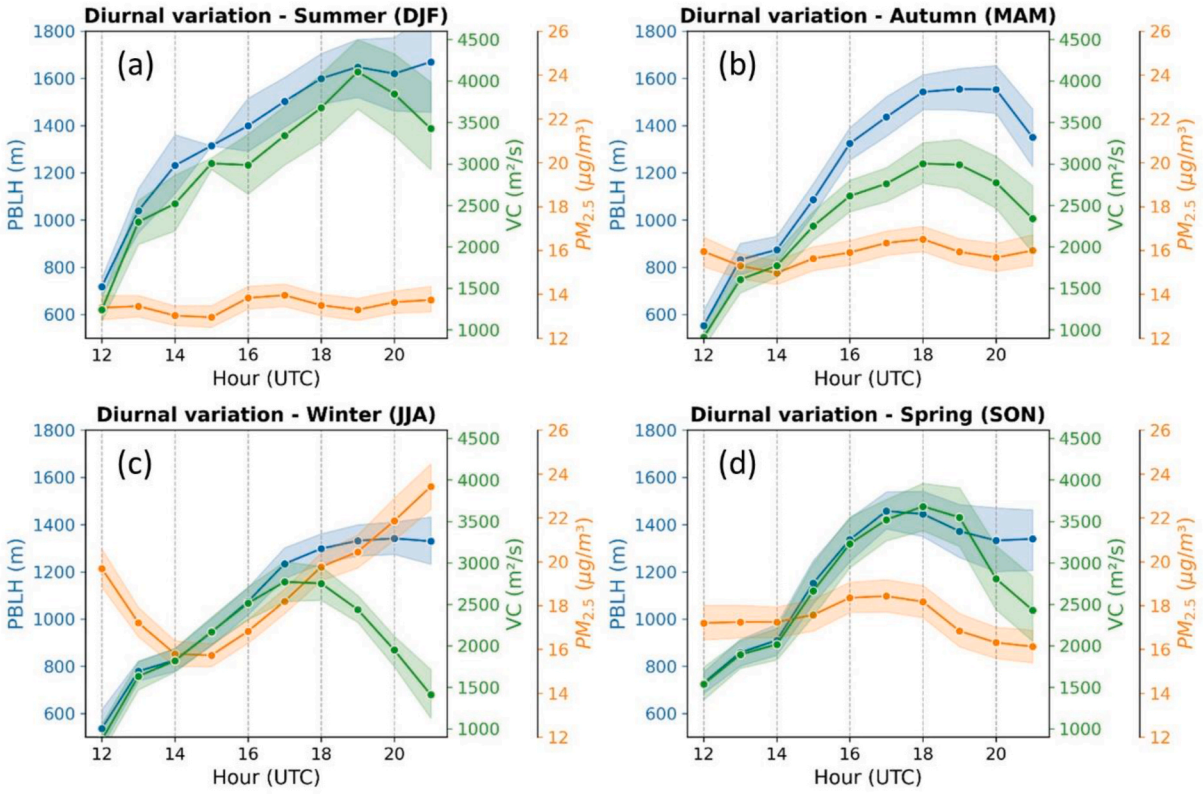

Fig. 9. Diurnal variation (14:00–21:00 UTC) for each season (a-Summer, b-Autumn, c-Winter, d-Spring) from March 2013 to November 2019 of *PBLH* (blue), *VC* (green) and $PM_{2.5}$ concentration (orange). Shaded regions show 95% confidence intervals.

could be observed when the $PM_{2.5}$ concentration was greater than 70 μgm^{-3}. Miao and Liu (2019), when analyzing the relationship between *PBLH* and $PM_{2.5}$ in China identified that during heavily polluted winters these variables had a correlation higher than 0.80, however when the $PM_{2.5}$ is lower than 50 μgm^{-3} small correlations were observed. Therefore, based on the studies presented above, it is possible to conclude that *PBLH* and $PM_{2.5}$ are well correlated only in the cases where the pollutant presents a high concentration, what justifies the low values observed in São Paulo city, because the average concentrations of $PM_{2.5}$ did not exceed 22 μgm^{-3} over the period analyzed.

On the other hand, *VC* presents a higher significative correlation where the higher value is observed in winter (−0.32) and lowest one in summer (−0.08). Su et al. (2018) observed a significative correlation between *HWS* and $PM_{2.5}$, then as *VC* is the combination of *PBLH* and *HWS*, such a variable tends to have a correlation higher than *PBLH*.

In an attempt to improve this correlation, and based on the relationship between *PBLH, VC, TI, AOD* and $PM_{2.5}$ demonstrated in previous sections, a Generalized Linear Model [*GLM*] (Nelder and Wedderburn, 1972) was created taking as input values the minimum, average and maximum daily values of all variables presented in this work. The dataset was split in two parts, so that the first 5 years (2013–2017) were applied to create the model and the last 2 years (2018–2019) were used to validate it. After creating an initial baseline model, variables with a low level of significance (p-value >0.05) were discarded. Such a *GLM* was adjusted with Poisson distribution and logarithmic link function (Dalgaard, 2008). Finally, the model had the following configuration:

$$PM_{2.5}^{Mean} = 3.45 + 0.55AOD + 0.06SBI_{Int} - 0.82VC_{Mean} + 0.01EI_{Base} \quad (4)$$

where: $PM_{2.5}^{Mean}$ and *AOD* corresponds to mean daily value of $PM_{2.5}$ and *AOD*, respectively, SBI_{Int} is the intensity of *SBI*, EI_{Base} is the height of *EI* base, and VC_{Mean} is the mean daily *VC*.

Fig. 11 presents a comparison between the $PM_{2.5}$ mean daily value measured and provided by the *GLM* model. were adjusted to Generalized Linear Models (GLMs) with Poisson distribution and logarithmic link function (Dalgaard, 2008). The model has a $R^2 = 0.93$ and a deviance [D^2] (how much of the variability of the variable is explained by the model) of 0.60. Liang et al. (2017), only combining atmospheric parameters, created a GLM that reached $R^2 = 0.81$. Liu et al. (2007), using *MODIS* data, created a *GLM* with $R^2 = 0.51$. On the other hand, Raman and Kumar (2016) combining meteorological parameters and some atmospheric optical properties developed a *GLM* that provide $R^2 = 0.88$. When comparing the model inputs, the need to insert information related to the optical properties of the atmosphere (e.g. *AOD*), thermal inversions (e.g., EI_{Base} and SBI_{Int}) and low troposphere dynamics (e.g., *VC*) becomes evident.

5. Conclusions

Air quality is a global issue that has a significant impact on major urban centers worldwide. It is crucial to comprehend the distinct attributes of each region and determine the factors that contribute to pollutants dispersion. In this scenario, the present study investigates as the seasonal variation of the *PBLH*, *VC*, *TI* occurrence, and *AOD* can influence the $PM_{2.5}$ concentration in São Paulo city during the convective period.

The *PBLH* observed in São Paulo city presents the maximum average values in summer and lower ones in winter. The seasonal average values of *PBLH* do not exhibit much variation as those seen in high latitude regions. Moreover, the sea breeze has a notable impact during the late afternoon, causing a reduction in aerosol concentration and an apparent decrease in *PBLH* estimated from lidar data. In addition, from a trend analysis it was possible to observe a tendency for increase in the $PBLH_{Max}$ during winter and autumn.

Regarding the *TI*, *EI* are more frequent than *SBI*, what is expected because he radiosounding were launched at 09 AM (Local Time). Winter

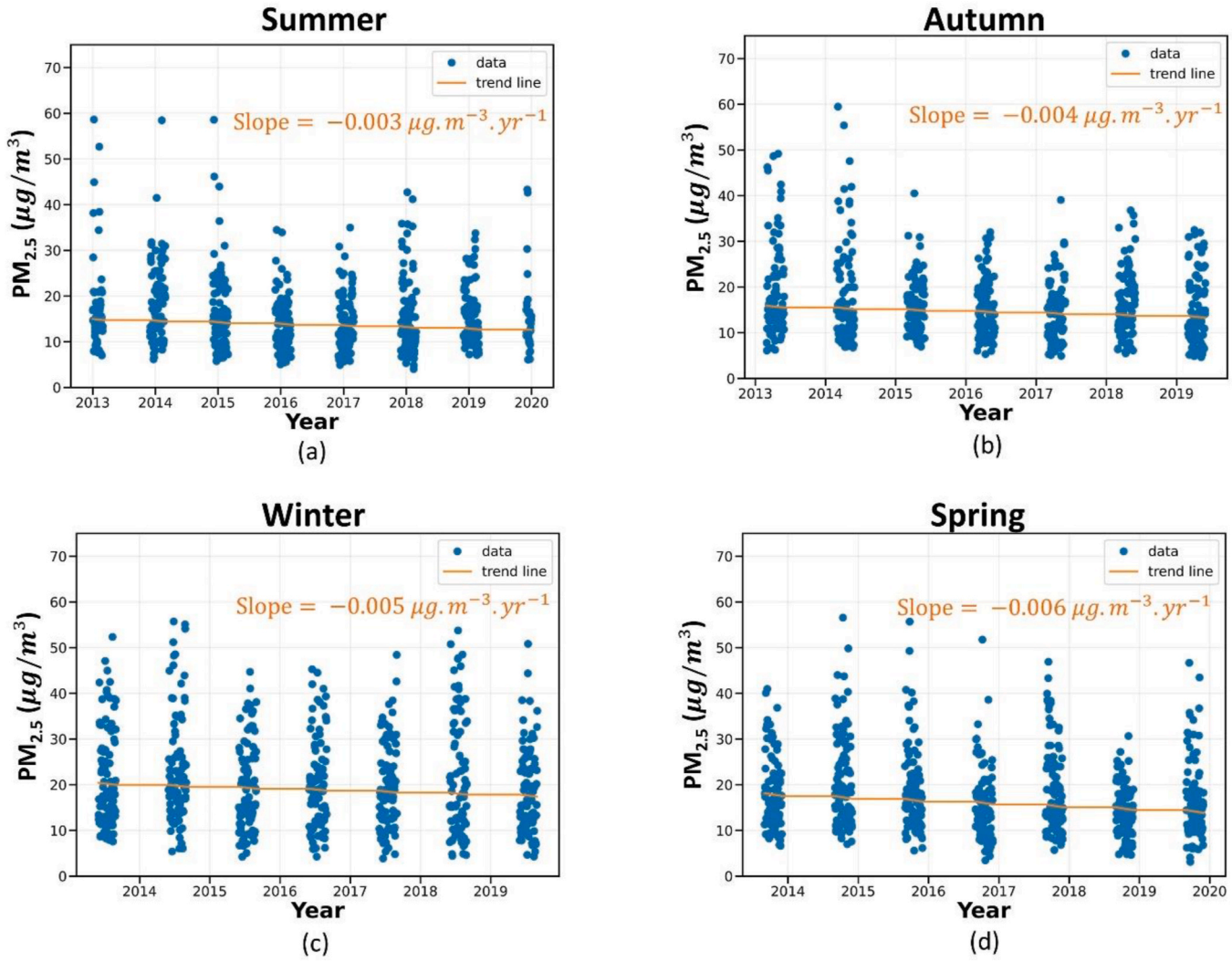

Fig. 10. Trend analyzes of the daily maximum value of $PM_{2.5}$ for the whole period (March 2013 to November 2019).

Table 2
Effect of *TI* in $PM_{2.5}$ concentration.

	$PM_{2.5}^{Min}$ (μgm^{-3})		$PM_{2.5}^{Mean}$ (μgm^{-3})		$PM_{2.5}^{Max}$ (μgm^{-3})	
	With *TI*	Without *TI*	With *TI*	Without *TI*	With *TI*	Without *TI*
Summer	6.2 ± 0.3	5.9 ± 0.2	14.1 ± 0.9	13.2 ± 0.2	24.7 ± 0.4	23.1 ± 0.5
Autumn	7.4 ± 0.5	8.1 ± 0.5	16.4 ± 1.2	16.9 ± 1.3	28.7 ± 0.5	28.7 ± 0.5
Winter	9.2 ± 0.2	8.4 ± 0.2	22.9 ± 0.4	22.4 ± 0.3	40.2 ± 0.6	3O.1 ± 0.3
Spring	7.8 ± 0.2	7.2 ± 0.1	17.4 ± 0.3	15.9 ± 0.2	30.4 ± 0.8	27.4 ± 0.4

Table 3
Pearson's correlation between $PM_{2.5}$ concentration, *VC* and *PBLH*. ** indicates a p-value lower than 0.05. * indicates a p-value lower than 0.1

Season	*VC*	*PBLH*
Winter	−0.32**	−0.05*
Autumn	−0.16**	−0.14*
Summer	−0.08**	−0.01
Spring	−0.20**	−0.11*

is the season with the deepest and most intense *EI* and, as they occur predominantly in the *PBL* region, they affect the *PBLH* growth rate and consequently the pollutant dispersion. Similarly to *PBLH*, the *VC* exhibits seasonal behavior, with higher average values during summer and lower ones during winter.

Based on the aerosol characterization using *AERONET* data, it was found that although each season has some distinct features regarding aerosol composition (e.g., winter is strongly impacted by biomass burning events in central-west and Amazonian Brazilian regions), small particles with low absorption and *BC* aerosol predominate throughout the year. Additionally, a negative correlation between *AOD* and *PBLH* was observed.

$PM_{2.5}$ also presents a seasonal behavior, with higher concentrations during the winter and lower ones in summer. In addition, from the trend analysis was possible to observe a tendency in reduction of the maximum $PM_{2.5}$ daily value concentration in all seasons. In general,

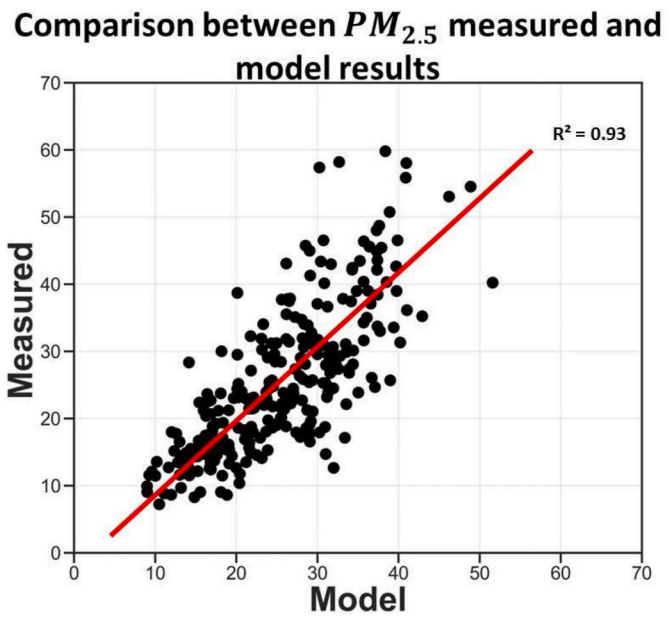

Fig. 11. Comparison between the $PM_{2.5}$ mean daily value measured and provided by the GLM.

$PM_{2.5}$ presented a low correlation with *PBLH*, demonstrating a small increase when the highest concentrations of $PM_{2.5}$ were observed. According to studies carried out in other locations (e.g., Beijing and Shenyang), similar results were found, so that high correlations (above 0.80) only were observed when $PM_{2.5}$ concentrations are higher than 50 μgm^{-3}. In São Paulo city the highest values observed to $PM_{2.5}$ concentration was 22 μgm^{-3}, what justifies the lower correlations observed. Although the correlations values between *VC* and $PM_{2.5}$ are better than those of the *PBLH* and $PM_{2.5}$, they are relatively low, and also rise according to increase of the $PM_{2.5}$ concentration.

The *GLM* proposed, combining information about *VC* [*PBLH* plus *HWS*], *TI* [SBI_{Int} and EI_{Base}] and optical properties [*AOD*], provided reasonable results [$R^2 = 0.93$ and $D^2 = 0.60$] in cases of intense and low PM2.5 concentration, demonstrating the importance of combining these three categories of data to better understand the dynamics of $PM_{2.5}$ dispersion.

This paper reinforced the importance of combining remote sensing and surface equipment to understand the $PM_{2.5}$ behavior, and although the variables when analyzed independently present a low degree of correlation with $PM_{2.5}$, when combined, significantly higher correlations levels could be achieved.

CRediT authorship contribution statement

Gregori de Arruda Moreira: Conceptualization, Data curation, Formal analysis, Investigation, Methodology, Resources, Software, Supervision, Validation, Visualization, Writing – original draft, Writing – review & editing. **Marcia Talita Amorim Marques:** Conceptualization, Data curation, Formal analysis, Funding acquisition, Methodology, Software, Writing – original draft, Writing – review & editing. **Fabio Juliano da Silva Lopes:** Data curation, Software. **Maria de Fátima Andrade:** Data curation, Funding acquisition. **Eduardo Landulfo:** Funding acquisition, Writing – original draft, Writing – review & editing.

Declaration of competing interest

The authors declare that they have no known competing financial interests or personal relationships that could have appeared to influence the work reported in this paper.

Acknowledgements

The authors are grateful to the State of São Paulo Environmental Company (CETESB) for making air quality and meteorological data available.

The authors thank the São Paulo Research Foundation (FAPESP) for the research grant n° 2019/17304-9 and the FAPESP thematic project 2016/18438-0.

References

Abdul-Wahab, S.A., Al-Saifi, S.Y., Alrumhi, B.A., Abdulraheem, M.Y., Al-Uraimi, M., 2004. Determination of the features of the low-level temperature inversions above a suburban site in Oman using radiosonde temperature measurements: long-term analysis. J. Geophys. Res. 109, D20101. https://doi:10.1029/2004JD004543.

Baars, H., Ansmann, A., Engelmann, R., Althausen, D., 2008. Continuous monitoring of the boundary-layer top with lidar. Atmos. Chem. Phys. 8 (3), 10749–10790. https://doi.org/10.5194/acp-8-7281-2008.

Bai, K., Ma, M., Chang, N.B., Gao, W., 2019. Spatiotemporal trend analysis for fine particulate matter concentrations in China using high-resolution satellite-derived and ground-measured PM2.5 data. J. Environ. Manag. 233, 530–542. https://doi.org/10.1016/j.jenvman.2018.12.071.

Bravo-Aranda, Juan Antonio, Moreira, De Arruda, Gregori, Navas-Guzmán, Francisco, Granados-Muñoz, José, María, Guerrero-Rascado, Luis, Juan, Pozo-Vázquez, David, Arbizu-Barrena, Clara, Reyes, Olmo, José, Francisco, Mallet, Marc, Arboledas, Alados, 2017. Lucas . A new methodology for PBL height estimations based on lidar depolarization measurements: analysis and comparison against MWR and WRF model-based results. Atmos. Chem. Phys. 17, 6839–6851.

Caicedo, V., Rappenglück, B., Lefer, B., Morris, G., Toledo, D., Delgado, R., 2017. Comparison of aerosol lidar retrieval methods for boundary layer height detection using ceilometer aerosol backscatter data. Atmos. Meas. Tech. 10, 1609–1622. https://doi.org/10.5194/amt-10-1609-2017.

Cazorla, A., Bahadur, R., Suski, K.J., Cahill, J.F., Chand, D., Schmid, B., Ramanathan, V., Prather, K.A., 2013. Relating aerosol absorption due to soot, organic carbon, and dust to emission sources determined from in-situ chemical measurements. Atmos. Chem. Phys. 13, 9337–9350. https://doi.org/10.5194/acp-13-9337-2013.

CETESB, 2019. Qualidade do Ar no Estado de São Paulo 2018. https://cetesb.sp.gov.br/ar/wp-content/uploads/sites/28/2019/07/Relat%C3%B3rio-de-Qualidade-do-Ar-2018.pdf. (Accessed 1 June 2021).

Chen, S., Tong, B., Russell, L.M., Wei, J., Guo, J., Mao, F., Liu, D., Huang, Z., Xie, Y., Qi, B., Zhang, H., Sun, Y., Zhang, B., Xu, C., Wu, L., Liu, D., 2022. Lidar-based daytime boundary layer height variation and impact on the regional satellite-based $PM_{2.5}$ estimate. Remote Sensing of Environment 281, 113224. https://doi.org/10.1016/j.rse.2022.113224.

Dalgaard, P., 2008. Introductory Statistics with R. Springer Science+Business Media, LLC, New York.

D'Amico, G., Amodeo, A., Mattis, I., Freudenthaler, V., Pappalardo, G., 2016. EARLINET Single Calculus Chain – technical – Part 1: pre-processing of raw lidar data. Atmos. Meas. Tech. 9, 491–507. https://doi.org/10.5194/amt-9-491-2016.

Dupont, J.-C., Haeffelin, M., Badosa, J., Elias, T., Favez, O., Petit, J.E., Meleux, F., Sciare, J., Crenn, V., Bonne, J.L., 2016. Role of the boundary layer dynamics effects on an extreme air pollution event in Paris. Atmos. Environ. 141, 571–579. https://doi.org/10.1016/j.atmosenv.2016.06.061.

Guo, J., Chen, X., Su, T., Liu, L., Zheng, Y., Chen, D., Li, J., Xu, H., Lv, Y., He, B., Li, Y., Hu, X., Ding, A., Zhai, P., 2020. The Climatology of lower tropospheric temperature inversions in China from radiosonde measurements: Roles of black carbon, local meteorology, and large-scale Subsidence. J. Clim. 33 (21), 9327–9350. https://doi.org/10.1175/JCLI-D-19-0278.1.

Holben, B., Eck, T., Slutsker, I., Tanré, D., Buis, J., Setzer, A., Vermote, E., Reagan, J., Kaufman, Y., Nakajima, T., Lavenu, F., Jankowiak, I., Smirnov, A., 1998. AERONET—a federated Instrument network and data Archive for aerosol characterization. Remote Sens. Environ. 66, 1–16.

IBGE, 2020. Instituto Brasileiro de Geografia e Estatística. http://ibge.gov.br. (Accessed 1 June 2021).

Kotthaus, S., Halios, C.H., Barlow, J.F., Grimmond, C.S.B., 2018. Volume for pollution dispersion: London's atmospheric boundary layer during ClearfLo observed with two ground-based lidar types. Atmos. Environ. 190, 401–414. https://doi.org/10.1016/j.atmosenv.2018.06.042.

Lee, J., Hong, J.W., Lee, K., et al., 2019. Ceilometer monitoring of boundary-layer height and its Application in Evaluating the Dilution effect on air pollution. Boundary-Layer Meteorol. 172, 435–455. https://doi.org/10.1007/s10546-019-00452-5.

Li, Z., Guo, J., Ding, A., Liao, H., Liu, J., Sun, Y., Wang, T., Xue, H., Zhang, H., Zhu, B., 2017. Aerosol and boundary-layer interactions and impact on air quality. Natl. Sci. Rev. 4 (6), 810–833. https://doi.org/10.1093/nsr/nwx117.

Li, X., Hu, X.M., Ma, Y., Wang, Y., Li, L., Zhao, Z., 2019. Impact of planetary boundary layer structure on the formation and evolution of air-pollution episodes in Shenyang, Northeast China. Atmos. Environ. 214, 116850.

Li, C., van Donkelaar, A., Hammer, M.S., et al., 2023. Reversal of trends in global fine particulate matter air pollution. Nat. Commun. 14, 5349. https://doi.org/10.1038/s41467-023-41086-z.

Liang, P., Zhu, T., Fang, Y., Li, Y., Han, Y., Wu, Y., Hu, Y., Wang, J., 2017. The role of meteorological condition and pollution control strategies in reducing air pollution in

Beijing during APEC 2014 and Victory Parade 2015. Atmos. Chem. Phys. 17, 13921–13940. https://doi.org/10.5194/acp-17-13921-2017.
Liu, B., Ma, Y., Guo, J., Gong, W., Zhang, Y., Mao, F., Li, J., Guo, X., Shi, Y., 2019. Boundary layer heights as derived from ground-based radar wind profiler in Beijing. IEEE Trans. Geosci. Rem. Sens. 57 (10), 8095–8104. https://doi.org/10.1109/TGRS.2019.2918301.
Liu, Y., Franklin, M., Kahn, R., Koutrakis, P., 2007. Using aerosol optical thickness to predict ground-level PM2.5 concentrations in the St. Louis area: a comparison between MISR and MODIS. Remote Sens. Environ. 107, 33–44. https://doi.org/10.1016/j.rse.2006.05.022, 2007.
Lopes, F.J.S., Silva, J.J., Antuña Marrero, J.C., Taha, G., Landulfo, E., 2019. Synergetic aerosol layer observation after the 2015 Calbuco Volcanic Eruption event. Remote Sens 11, 195. https://doi.org/10.3390/rs11020195.
Lou, M., Guo, J., Wang, L., Xu, H., Chen, D., Miao, Y., Lv, Y., Li, Y., Guo, X., Ma, S., Li, J., 2019. On the relationship between aerosol and boundary layer height in summer in China under different thermodynamic conditions. Earth Space Science. 6 (5), 887–901. https://doi.org/10.1029/2019EA000620.
Lu, C., Deng, Q.H., Liu, W.W., Huang, B.L., Shi, L.Z., 2012. Characteristics of ventilation coefficient and its impact on urban air pollution. J. Cent. S. Univ. 19 (3), 615–622. https://doi.org/10.1007/s11771-012-1047-9.
Luan, T., Guo, X., Guo, L., Zhang, T., 2018. Quantifying the relationship among PM2.5 concentration, visibility and planetary boundary layer height for long-lasting haze and fog-haze mixed events in Beijing City. Atmos. Chem. Phys. https://doi.org/10.5194/acp-18-203-2018.
Marques, Márcia T.A., Moreira, Gregori De A., Pinero, Maciel, Oliveira, Amauri P., Landulfo, Eduardo, 2018. Estimating the planetary boundary layer height from radiosonde and Doppler lidar measurements in the city of São Paulo - Brazil. EPJ Web Conf. 176, 06015 https://doi.org/10.1051/epjconf/201817606015.
Miao, Y., Liu, S., 2019. Linkages between aerosol pollution and planetary boundary layer structure in China. Sci. Total Environ. 650, 288–296. https://doi.org/10.1016/j.scitotenv.2018.09.032.
Moreira, G.A., Lopes, F.J. da S., Guerrero-Rascado, J.L., Granados-Muñoz, M.J., Bourayou, R., Landulfo, E., 2014. Comparison between two algorithms based on different wavelets to obtain the Planetary Boundary Layer height. Proc. SPIE 9246, Lidar Technologies, Techniques, and Measurements for Atmospheric Remote Sensing X, 92460D. https://doi.org/10.1117/12.2067352.
Moreira, G.A., Guerrero-Rascado, J.L., Bravo-Aranda, J.A., Benavent-Oltra, J.A., Ortiz-Amezcua, P., Róman, R., Bedoya-Velásquez, A.E., Landulfo, E., Alados-Arboledas, L., 2018. Study of the planetary boundary layer by microwave radiometer, elastic lidar and Doppler lidar estimations in Southern Iberian Peninsula. Atmos. Res. 213, 185–195. https://doi.org/10.1016/j.atmosres.2018.06.007.
Moreira, G.A., Andrade, I.S., Cacheffo, A., da Silva Lopes, F.J., Calzavara Yoshida, A., Gomes, A.A., da Silva, J.J., Landulfo, E., 2021. Influence of a Biomass-Burning Event in $PM_{2.5}$ Concentration and Air Quality: A Case Study in the Metropolitan Area of São Paulo. Sensors 21, 425. https://doi.org/10.3390/s21020425.
Moreira, G.A., Guerrero-Rascado, J.L., Benavent-Oltra, J.A., Ortiz-Amezcua, P., Román, R., Bedoya-Velásquez, A.E., Bravo-Aranda, J.A., Olmo-Reyes, F.J., Landulfo, E., Alados-Arboledas, L., 2019. Analyzing the turbulent planetary boundary layer by remote sensing systems: the Doppler wind lidar, aerosol elastic lidar and microwave radiometer. Atmos. Chem. Phys. 19, 1263–1280, 2019.
Moreira, G.A., Guerrero-Rascado, J.L., Bravo-Aranda, J.A., Foyo-Moreno, I., Cazorla, A., Alados, I., Lyamani, H., Landulfo, E., Alados-Arboledas, L., 2020. Study of the planetary boundary layer height in an urban environment using a combination of microwave radiometer and ceilometer. Atmos. Res. 240, 104932 https://doi.org/10.1016/j.atmosres.2020.104932.
Moreira, G.A., Oliveira, A.P., Sánchez, M.P., Codato, G., Lopes, F.J. da S., Landulfo, E., Filho, E.P.M., 2022. Performance assessment of aerosol-lidar remote sensing skills to retrieve the time evolution of the urban boundary layer height in the Metropolitan Region of São Paulo City, Brazil. Atmos. Res. 277, 106290 https://doi.org/10.1016/j.atmosres.2022.106290.
Murthy, B.S., Latha, R., Tiwari, A., Rathod, A., Singh, S., Beig, G., 2020. Impact of mixing layer height on air quality in winter. J. Atmos. Sol. Terr. Phys. 197, 105157–105826. https://doi.org/10.1016/j.jastp.2019.105157.
Nair, V.S., Moorthy, K.K., Alappattu, D.P., Kunhikrishnan, P.K., George, S., Nair, P.R., Babu, S.S., Abish, B., Satheesh, S.K., Tripathi, S.N., Niranjan, K., 2007. Wintertime aerosol characteristics over the Indo-Gangetic Plain (IGP): Impacts of local boundary layer processes and long-range transport. J. Geophys. Res. Atmos. 112 (D13) https://doi.org/10.1029/2006JD008099.
Nelder, J.A., Wedderburn, R.W.M., 1972. Generalized linear models. J R Stat Soc A 35, 370–384.
Oliveira, A.P., Bornstein, R.D., Soares, J., 2003. Annual and diurnal wind patterns in the city of São Paulo. Water. Air Soil Pollut 3 (5–6), 3–15.
Pal, S., Haeffelin, M., 2015. Forcing mechanisms governing diurnal, seasonal, and interannual variability in the boundary layer depths: five years of continuous lidar observations over a suburban site near Paris. J. Geophys. Res.-Atmos. 120 (11) https://doi.org/10.1002/2015JD023268, 936–11,956.
Pan, L., Xu, J., Tie, X., Mao, X., Gao, W., Chang, L., 2019. Long-term measurements of planetary boundary layer height and interactions with $PM_{2.5}$ in Shanghai, China. Atmos. Pollut. Res. 10, 989–996. https://doi.org/10.1016/j.apr.2019.01.007.
Raman, R.S., Kumar, S., 2016. First measurements of ambient aerosol over an ecologically sensitive zone in Central India: relationships between PM2.5 mass, its optical properties, and meteorology. Sci. Total Environ. 550, 706–716. https://doi.org/10.1016/j.scitotenv.2016.01.092.
Ribeiro, F.N.D., Oliveira, A. P. de, Soares, J.R., Miranda, R. M. de, Barlage, M., Chen, F., 2018. Effect of sea breeze propagation on the urban boundary layer of the metropolitan region of São Paulo, Brazil. Atmos. Res. 214, 174–188. https://doi.org/10.1016/j.atmosres.2018.07.015.
Romano, S., Perrone, M.R., Pavese, G., Esposito, F., Calvello, M., 2019. Optical properties of PM2.5 particles: results from a monitoring campaign in southeastern Italy. Atmos. Environ. 203, 35–47. https://doi.org/10.1016/j.atmosenv.2019.01.037.
Salmun, H., Josephs, H., Molod, A., 2023. GRWP-PBLH: global radar wind profiler planetary boundary layer height data. Bull. Amer. Meteor. Soc. 104, E1044–E1057. https://doi.org/10.1175/BAMS-D-22-0002.1.
Sánchez, M.P., de Oliveira, A.P., Varona, R.P., Tito, J.V., Codato, G., Ribeiro, F.N.D., Marques Filho, E.P., Silveira, L.C.d., 2020. Rawinsonde-based analysis of theurban boundary layer in the metropolitan region of São Paulo ,Brazil. Earth Space Sci. 7, e2019EA000781 https://doi.org/10.1029/2019EA000781.
São Paulo, 2020. Municipality. https://www.prefeitura.sp.gov.br/. (Accessed 1 June 2021).
Schween, J.H., Hirsikko, A., Löhnert, U., Crewell, S., 2014. Mixing-layer height retrieval with ceilometer and Doppler lidar: from case studies to long-term assessment. Atmos. Meas. Tech. 7 (11), 3685–3704.
Seinfield, J.H., Pandis, S.N., 2016. Atmospheric Chemistry and Physics: From air Pollution to Climate Change, 3rd edition. Wiley, Hoboken.
Sen, P.K., 1986. Estimates of the regression coefficient based on Kendall's tau. J. Am. Stat. Assoc. 63, 1379–1389.
Solanki, R., Guo, J., Lv, Y., Zhang, J., Wu, J., Tong, B., Li, J., 2022. Elucidating the atmospheric boundary layer turbulence by combining UHF radar wind profiler and radiosonde measurements over urban area of Beijing. Urban Clim. 43, 101151 https://doi.org/10.1016/j.uclim.2022.101151.
Stull, R.B., 1988. An Introduction to Boundary Layer Meteorology. Kluwer Acad., Dordrecht, Netherlands, p. 666.
Su, T., Li, Z., Kahn, R., 2018. Relationships between the planetary boundary layer height and surface pollutants derived from lidar observations over China: regional pattern and influencing factors. Atmos. Chem. Phys. 18, 15921–15935. https://doi.org/10.5194/acp-18-15921-2018.
Teixeira, J., Piepmeier, J.R., Nehrir, A.R., Ao, C.O., Chen, S.S., Clayson, C.A., Fridlind, A. M., Lebsock, M., McCarty, W., Salmun, H., Santanello, J.A., Turner, D.D., Wang, Z., Zeng, X., 2021. Toward a Global Planetary Boundary Layer Observing System: the NASA PBL Incubation Study Team Report. NASA PBL Incubation Study Team.
Toledo, D., Córdoba-Jabonero, C., Adame, J.A., Benito, D.L.M., Gil-Ojeda, M., 2017. Estimation of the atmospheric boundary layer height during different atmospheric conditions: a comparison on reliability of several methods applied to lidar measurements. Int. J. Remote Sens. 38, 3203–3218.
Uzan, L., Egert, S., Khain, P., Levi, Y., Vadislavsky, E., Alpert, P., 2020. Ceilometers as planetary boundary layer height detectors and a corrective tool for COSMO and IFS models. Atmos. Chem. Phys. 20, 12177–12192. https://doi.org/10.5194/acp-20-12177-2020.
Wallace, J., Kanaroglou, P., 2009. The effect of temperature inversions on ground level nitrogen dioxide (NO2) and fine particulate matter ($PM_{2.5}$) using temperature profiles from the Atmospheric Infrared Sounder (AIRS). Sci. Total Environ. 407, 5085–5095.
Xiang, Y., Zhang, T., Liu, J., Lv, L., Dong, Y., Chen, Z., 2019. Atmosphere boundary layer height and its effect on air pollutants in Beijing during winter heavy pollution. Atmos. Res. 215, 305–316. https://doi.org/10.1016/j.atmosres.2018.09.014.
Xu, T., Song, Y., Liu, M., Cai, X., Zhang, H., Guo, J., Zhu, T., 2019. Temperature inversions in severe polluted days derived from radiosonde data in North China from 2011 to 2016. Sci. Total Environ. 647, 1011–1020. https://doi.org/10.1016/j.scitotenv.2018.08.088.
Lopes, F.J.S., 2021. AERODOG - AERONET Data Organization & Graphics. Github. Available at: https://github.com/inciteleal/aerodog_incite.